Estimation of the fracture toughness of tungsten fibre-reinforced tungsten composites

H. Gietl[a,b], S. Olbrich[a], J. Riesch[a], G. Holzner[a,b], T. Höschen[a], J.W. Coenen[c,d], R. Neu[a,b]

[a] *Max-Planck-Institut für Plasmaphysik, Boltzmannstrasse 2, 85748 Garching, Germany*
[b] *Technische Universität München, Boltzmannstrasse 15, 85748 Garching, Germany*
[c] *Forschungszentrum Jülich GmbH, Institut für Energie und Klimaforschung, Partner of the Trilateral Euregio Cluster (TEC), 52425 Juelich,Germany*
[d] *Department of engineering physics, University of Wisconsin Madison, WI 53706 Madison, USA*

Abstract

Tungsten fibre-reinforced tungsten composites (W_f/W) have been developed to overcome the inherent brittleness of tungsten, which is a promising candidate for the plasma-facing material in a future fusion power plant. As the development of W_f/W evolves, the fracture toughness of the composite is in the focus of interest for further component design. In this contribution fracture mechanical tests on two different types of chemical vapour deposited (CVD) W_f/W are presented. Three-point bending tests according to ASTM E399 as a standard method for brittle materials were used to get a first estimation of the toughness. A provisional fracture toughness value of up to 241 MPa $m^{1/2}$ was calculated for the as-fabricated and of up to 20.5 MPa $m^{1/2}$ for a heat-treated and thus embrittled state. As the material does not show a brittle fracture in the as-fabricated state, the J-Integral approach based on the ASTM E1820 was additionally applied for this state. A maximum value of the J-integral of 7.5 kJ/m^2 (57.6 MPa $m^{1/2}$) was determined. A detailed post mortem investigations was used to obtain the active mechanisms.

Keywords: tungsten, tungsten fibre, fibre-reinforced composite, metal matrix composite, fracture toughness

1. Introduction

The ideal material for highly loaded areas in a future fusion device needs to combine properties such as low sputter yield, high melting point, high thermal conductivity and moderate activation [3]. Tungsten (W), as a promising candidate for such structures, in addition also features high strength and creep resistance at elevated temperatures. However, the inherent brittleness below the ductile-to-brittle transition temperature (DBTT) [4, 5] and the embrittlement during operation, e.g. by overheating [6] and/or neutron irradiation [7, 8] are the main drawbacks for the use of pure W. To overcome this limitation, tungsten fibre-reinforced tungsten composites (W_f/W) have been developed. Besides short fibre reinforced W_f/W produced with a powder metallurgical process [9, 10], a promising production route for W_f/W reinforced with continuous fibres is a layered chemical vapour deposition (CVD) process [11, 12]. The composites utilise extrinsic mechanisms to improve the toughness [13, 14], similar to ceramic fibre-reinforced ceramics [15]. These mechanisms work for as-fabricated conditions of W_f/W [13], as well as for embrittled material [16]. A layerwise chemical vapour (CVD) deposition process was used to produce bulk samples [12]. Enhanced performance in comparison to bulk W was shown for this CVD long fibre-reinforced W composites [12, 16, 17]. In this contribution, we give a detailed description of the evaluation of the fracture toughness of W_f/W with three-point-bending tests. Two different three point bending test set-ups and an optical measurement system for real time displacement evaluation and crack observation were used. A first estimation of the toughness is given by utilising three-point-bending tests according to ASTM E399 [2]. Similar to studies on other W based materials [18] a provisional fracture toughness (K_P) was calculated. For a quantitative evaluation the J-Integral approach [19] typically used for tough materials according to ASTM E1820 [1] (J_Q) was applied on KLST-type W_f/W samples [20]. Sequential loading and partial unloading allows the observation of the crack growth and the calculation of the J-Integral at various crack lengths [21]. This was supplemented by microstructural investigations of the fracture surfaces to obtain the active mechanisms. Finally, the microstructural findings, the results as well as the applicability of the ASTM E399 and ASTM E1820 for W_f/W are critically discussed.

2. Material synthesis, sample preparation and experimental procedure

The bulk W_f/W investigated in this work was produced with a layerwise chemical vapor deposition process at approximately 650 °C described in [12]. Two types of unidirectional reinforced composite were produced. The first type had pure W fibres with a diameter of 150 μm [22] which were coated with a 1 μm erbia interlayer produced with magnetron sputtering according to [23]. This composite is called $W_f/W_{Er_2O_3}$ in the following and had a fiber distance in every direction of around 120 μm with a fibre volume fraction between 21 and 22% . The density was measured to be between 91.2 and 92.5 % using a cross-section image. This method uses a processed microscopy image to distinguish between the pores (converted to black) and the dense material (converted to white) by calculating the black and white pixels within that image. The second composite

Nomenclature

η_{pl}	function of the crack length in comparison to the original specimen height
γ_{pl}	function of the crack length in comparison to the original specimen height
ν	Poisson's ratio
a	crack length
$a_{initial}$	initial length of the crack
$a_{opening}$	crack opening (measured for all $W_f/W_{Y_2O_3}$ specimens)
$a_{surface}$	the surface crack length at the front side of the K_P specimens
$f(a/H)$	dimensionless function defined in the standard
K_{QJ}	stress intensity factor
A_{pl}	area under the load-displacement curve without the elastic part calculated from the slope of the curve
B	specimen thickness
CLSM	confocal laser scanning microscope
CVD	chemical vapour deposition
DBTT	ductile-to-brittle transition temperature
E	Young's modulus
EDM	electrical discharge machining
Er_2O_3	erbium oxide
H	specimen height
index i	cycle number
J_{el}	elastic part of the J-Integral
J_{pl}	plastic part of the J-Integral
$J_{Q-initial}$	J-Integral value for crack initiation
J_{Q-max}	maximum J-Integral value
J_Q or J_i	provisional fracture toughness calculated according to ASTM E1820 [1]
K_{IC}	fracture toughness
$K_{J-0.2}$	provisional fracture toughness calculated with the J_Q values at a crack length of 0.2 mm
$K_{J-1.5}$	provisional fracture toughness calculated with the J_Q values at a crack length of 1.5 mm
K_{J-max}	provisional fracture toughness calculated with J_{Q-max}
$K_{P_{initial}}$	K_P calculated with $a_{initial}$
$K_{P_{surface}}$	K_P calculated with $a_{surface}$
K_P	provisional fracture toughness calculated according to ASTM E399 [2]
P	load applied to the specimen (K_P evaluation)
P_{max}	maximum load during bending test (K_{max} evaluation)
P_Q	load values before the first significant load-drop (K_P evaluation)
R-Curve	resistance-curve
S	span of three point bending test
W	tungsten
W_f/W	tungsten fibre-reinforced tungsten composite
$W_f/W_{Er_2O_3}$	W_f/W with erbia interlayer used for K_P evaluation in as-fabricated and annealed state
$W_f/W_{Y_2O_3}$	W_f/W with yttria interlayer used for K_P and J_Q evaluation in as-fabricated state and K_P evaluation in annealed state
Y_2O_3	yttrium oxide

type was produced using W fabrics [12, 24] consisting of K-doped W fibres with a diameter of 150 μm [25, 26] as warp fibre and 50 μm as weft fibre with a fiber distance in every direction of around 230 μm. This W fabrics were coated with a 1 μm thick yttria interlayer by magnetron sputtering according to [27]. This material is called $W_f/W_{Y_2O_3}$ in the following. $W_f/W_{Y_2O_3}$ had an optical density measured by image analysis between 94.1 and 99.8 % and a fibre volume fraction between 11 and 13 %.
Two different types of sample geometries were used for the fracture toughness testing. All specimens were cut out from a bigger bulk sample with electrical discharge machining (EDM) followed by polishing on all sides to remove EDM induced cracks. In Fig. 1 the sample geometry (with the fibre orientation indicated in red) which was used for K_P-tests is shown.

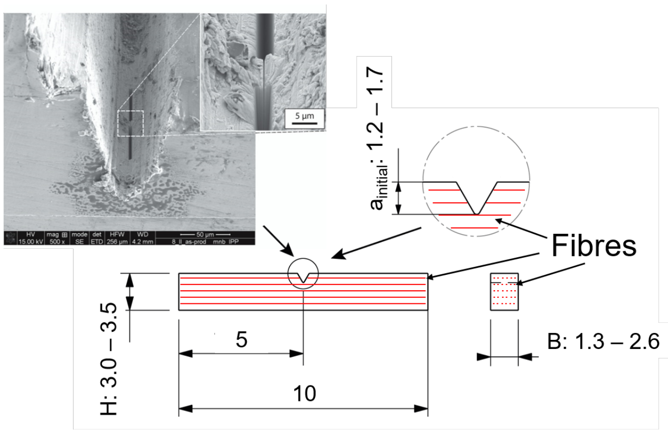

Figure 1: Bending specimen and artificial notch according to [18] for the samples tested according to ASTM E399. All dimensions are given in mm.

For the J_Q-testing KLST type [20] samples were used (see

Fig. 2).

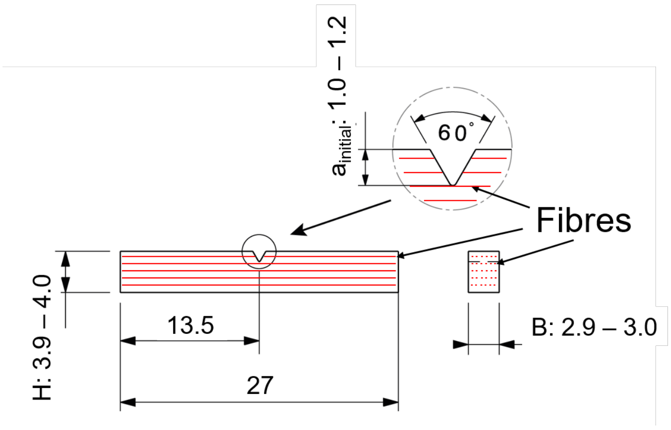

Figure 2: KLST - type geometry used for the J_Q evaluation according to ASTM E1820. All dimensions are given in mm. The W fibres are indicated in red.

An artificial sharp notch was used as pre-crack for all specimens, as fatigue pre-cracking was not possible due to the brittleness of the W-CVD matrix [18]. For all samples, at first, a notch was cut with a diamond wire saw with a wire diameter of 0.3 mm. For the $W_f/W_{Er_2O_3}$-K_P specimens this was followed by a razor blade polishing and a final Focused Ion Beam (FIB) milling with a depth of 8.8 - 16.5 μm similar as descried [18]. Such a notch is shown for in Fig. 1. For the $W_f/W_{Y_2O_3}$-K_P specimens and all KLST samples the diamond wire sawing was followed by wire sawing with a 0.03 mm thick W wire lubricated with a diamond particle oil suspension (average particle size 0.001 mm). The $W_f/W_{Y_2O_3}$-K_P samples were then FIB cut similar to the $W_f/W_{Er_2O_3}$-K_P specimens. The KLST - $W_f/W_{Y_2O_3}$-J_Q specimens had a dual step wire sawing with a second wire diameter of 0.03 mm with diamond oil suspension (average size of diamond-particles: 0.001 mm). After the first tests it was seen that the FIB milling was not necessary for the as-fabricated KLST samples as the crack growth always starts in the middle of the prepared notch. In addition, the notch refinement with the 0.03 mm wire saw had the same effect as the refinement with the razor blade and the change is caused by the lack of access to the razor blade notching machine. The overview of the notch preparation procedures is given in Tab. 1.

Table 1: Notch preparation procedures.

Step	$W_f/W_{Er_2O_3}$-K_P	$W_f/W_{Y_2O_3}$-K_P	$W_f/W_{Y_2O_3}$-J_Q
1	EDM	EDM	EDM
2	wire saw (Ø0.3 mm)	wire saw (Ø0.3 mm)	wire saw (Ø0.3 mm)
3	razor blade	wire saw (Ø0.03 mm)	wire saw (Ø0.03 mm)
4	FIB-cut	FIB-cut	–

Both sample geometries (K_P and J_Q) were tested in as-fabricated conditions and K_P samples were also tested after high temperature annealing, i.e. embrittlement. The annealing was performed after the cutting, polishing and notch preparation in a carbon oven and the samples were placed in tantalum envelopes to protect the W against carbonisation, as carbonisation leads to embrittlment and tungsten carbide formation as undesirable side effects [28]. The annealing led to an embrittlement of the fibres by massive grain growth [5, 18] and thus allowed the study of the effect of operational embrittlement. The different temperature treatments results from the use of pure [22] and K-doped W fibres [26] with different embrittlement temperatures. The $W_f/W_{Er_2O_3}$ samples were heated to 1800 °C and $W_f/W_{Y_2O_3}$ samples to 2200 °C. Both annealing temperatures were held for 0.5 h. The overview of the material types and usage is given in Tab. 2.

The tests were performed with an universal testing device (TIRAtest 2820, No. R050/01, TIRA GmbH) at room temperature (RT). To determine displacement and crack growth on the surface, the load-displacement curves were correlated to an optical surface observation. For the optical surface observation an optical measurement system with a telecentric lens (OPTO ENGINEERING - TC4 M004-C) with a four times magnification was used in combination with a monochrome digital camera (Toshiba - Typ DU657M). For all K_P tests a 5 kN load cell was used, while for the J_Q approach a 20 kN load cell was used.

2.1. Experiments according to ASTM E399 (K_P)

The fracture toughness values were calculated by analysis of load-displacement curves, according to ASTM E399 with the following equation:

$$K_P = \frac{P \cdot S}{B \cdot H^{3/2}} \cdot f(a/H) \qquad (1)$$

Where K_P is a provisional fracture toughness, P is the load applied to the specimen, S is the span (8 mm), B is the thickness, H is the height, a is the crack length and $f(a/H)$ is a dimensionless function defined in the standard. K_P is for this specimen geometry defined as K_{IC} if two size criteria are fulfilled according to [2]. The first one defines the specimen height - crack length ratio ($0.45 \leq a/H \leq 0.55$). The second size criterion defines the crack length a and the specimen thickness B. Both have to be larger than $2.5 \cdot (K_P/\sigma_y)^2$.

The determination of the crack length /a is complicated as the crack at the surface does not necessarily represent the real crack length in an inhomogeneous material like W_f/W [29]. Therefore, the initial length of the notch (artificial crack) $a_{initial}$ was used to calculate the provisional fracture toughness $K_{P_{initial}}$ as a conservative estimation, because longer crack lengths necessarily lead to higher fracture toughness values. The surface crack length $a_{surface}$ of the front side was used to calculate the more realistic $K_{P_{surface}}$. In addition, the crack opening $a_{opening}$ was measured for all $W_f/W_{Y_2O_3}$ samples. In Fig. 3 $a_{initial}$, $a_{surface}$ and $a_{opening}$ are indicated on a fractured sample.

The values of size, material combination, state, initial surface crack length and final surface crack length, for the specimens used for the K_P evaluation are summarized in Tab. 3.

The tests were performed with a constant displacement rate of 0.5 μm/s.

Table 2: Material types and usage.

test method	material	W-fibre	material state	heat treatment
K_P (ASTM E399)	$W_f/W_{Er_2O_3}$	pure	as-fabricated & annealed	1800 °C, 0.5 h
	$W_f/W_{Y_2O_3}$	K-doped	as-fabricated & annealed	2200 °C, 0.5 h
J_Q (ASTM E1820)	$W_f/W_{Y_2O_3}$	K-doped	as-fabricated	-

Table 3: Set of 3PB specimens for K_P estimation (ASTM E399) of two composites with and without heat treatment.

No.	State	Interlayer	B [mm]	H [mm]	$a_{initial}$ [mm]	$a_{ini.}$/H	$a_{surface}$ [mm]	$a_{sur.}$/H	P_{max} [N]	$K_{P_{ini.}}$ [MPa m$^{1/2}$]	K_{max} [MPa m$^{1/2}$]	$K_{P_{sur.}}$ (P_Q) [MPa m$^{1/2}$]
1	as-fab	Er_2O_3	2.3	3.4	1.7	0.5	2.8	0.8	883	39.6	190	
2	as-fab	Er_2O_3	2.3	3.5	1.7	0.4	2.9	0.8	585	25.5	130	
3	emb	Er_2O_3	1.9	3.4	1.3	0.4	1.6	0.5	155	6.1	8.0	
4	emb	Er_2O_3	2.2	3.4	1.3	0.4	2.0	0.6	294	10.2	18.3	
5	emb	Er_2O_3	2.2	3.0	1.2	0.4	1.9	0.6	198	9.1	20.5	
6	as-fab	Y_2O_3	2.0	3.4	1.3	0.4	2.9	0.9	603	23.0	215	144 (452 N)
7	as-fab	Y_2O_3	2.6	3.4	1.2	0.4	2.9	0.9	538	15.2	162	133 (460 N)
8	as-fab	Y_2O_3	2.0	3.4	1.2	0.4	2.9	0.9	611	22.3	241	167 (516 N)
9	emb	Y_2O_3	1.6	3.4	1.4	0.4	2.1	0.6	154	7.6	14.8	
10	emb	Y_2O_3	2.0	3.4	1.7	0.5	2.2	0.7	155	8.0	15.0	
11	emb	Y_2O_3	1.3	3.4	1.7	0.5	2.6	0.7	89	7.1	13.6	

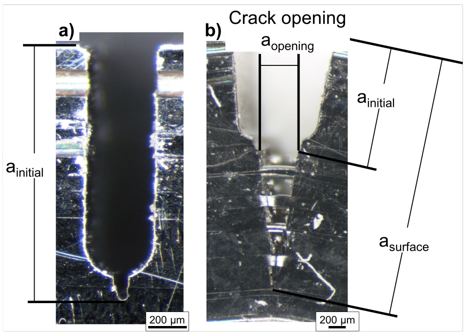

Figure 3: Initial, surface crack length and crack opening of typically K_P sample (specimen No.6).

2.2. Experiments according to ASTM E1820 (J_Q)

The J-Integral in the original sense is a path independent value of the stress concentration around, but excluding the crack tip [19]. The path independence only holds for straight cracks in homogenous materials with unloaded crack surfaces [30]. By taking the whole amount of energy absorbed by the specimen into account, one can calculate a global J-Integral even for composites [31]. The loading of the crack surface has to be taken into account, too. This is due to the fact, that the energy absorbed within a composite material is not only in the crack tip but also behind the matrix crack tip, where delamination pull-out, fibre-straining and fibre-fracture occurs.

The J_Q values, given in this paper, are evaluated based the single-specimen method given in ASTM E1820. The specimens are cyclically loaded and unloaded, to calculate J_Q values for different crack lengths precisely different crack resistances. In this case the cyclic loading is displacement controlled. The loading with an average displacement of 8 μm is higher than the unloading with an average of 3 μm and therefore an increasing load is applied to the specimen. This unloading compliance method is a common single-specimen test technique to determine a J-R curve [21]. The test was performed with a constant displacement rate of 0.5 μm/s.

The J-Integral is calculated as an elastic J_{el} and a plastic J_{pl} part, as defined in ASTM E1820 as follows:

$$J_{(i)} = J_{el(i)} + J_{pl(i)} \tag{2}$$

$$J_{el(i)} = \frac{(K_{(i)})^2 \cdot (1 - \nu^2)}{E} \tag{3}$$

$$\begin{aligned} J_{pl(i)} = {} & [J_{pl(i-1)} + (\frac{\eta_{pl(i-1)}}{b_{(i-1)}})(\frac{A_{pl(i)} - A_{pl(i-1)}}{B})] \\ & \times [1 - \gamma_{pl(i-1)}(\frac{a_{(i)} - a_{(i-1)}}{b_{(i-1)}})] \end{aligned} \tag{4}$$

With the provisional $J_{(i)}$ which is called J_Q in the following, a stress intensity factor K_J can be calculated as follows [1]:

$$K_J = \sqrt{\frac{J_Q E}{(1 - \nu^2)}} \tag{5}$$

Whereby

$$B > 10 \frac{J_Q}{\sigma_y} \tag{6}$$

is the size criterion for a valid test. K_J is the stress intensity factor calculated as described above with the span of 25 mm. η_{pl} and γ_{pl} are functions of the crack length in comparison to the original specimen height, A_{pl} is the area under the load-displacement curve without the elastic part calculated from the slope of the curve, E is the Young's modulus and ν is the materials Poisson's ratio. The index i indicates the cycle number. The crack length for the calculation is idealized from $a_{initial}$ as

zero crack propagation to the final crack length as it cannot exactly be determined in an inhomogeneous material as explained before. Heat tinting, known from steels and proposed in the ASTM E1820, could not be applied as W shows strong oxidation with material losses. Instead, the final crack length was marked trough thermoplastic infiltration. After the infiltration of a thermoplastic the samples were cooled down with liquid nitrogen and fully opened with an unilateral impact-stress (hammer).
The fracture surface was then investigated in an optical microscope and with a confocal laser scanning microscope (CLSM). The crack length formed during the test was measured on nine equally spaced positions for each sample. The nine white arrows in Fig. 4 b) indicate the final crack length for that sample after the test. The red line indicates the crack tip for this sample while in Fig. 4 a) and c) the back and front surface of the sample is shown.
As stable crack propagation was observed, equal steps between initial and final crack length were chosen to correlate crack propagation from the crack start and the end of the experiment. The initial crack length is the notch depth and the final crack length is the average crack length measured at nine positions as described before.

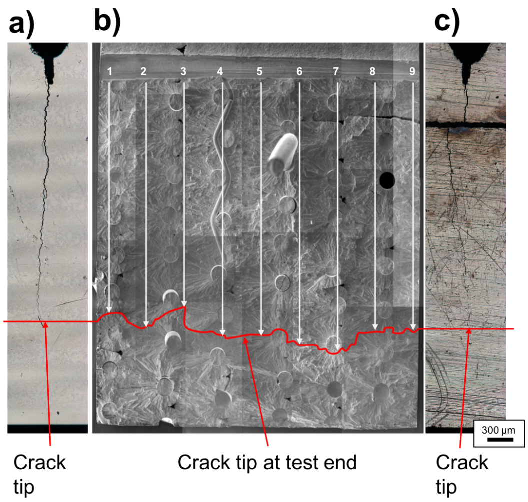

Figure 4: Crack length measurement of typically J_Q sample (specimen No. 13): Back side a), fracture surface b), front side c).

The specimen dimensions and the values for the initial and final crack lengths are given in Tab. 4. In addition, the crack opening $a_{opening}$ was measured at the end of experiment according to Fig. 3.

3. Results

3.1. Fracture toughness according to ASTM E399 (K_P)

Representative load-displacement diagrams, are shown for an as-fabricated specimen (No. 6) in Fig. 5 and an embrittled specimen (No. 9) in Fig. 6. In both curves a non-linear region is observed at the beginning caused by the setting of the testing setup. The linear loading of the as-fabricated samples is followed by a load drop (at 220 N) (Fig. 5). The second larger load drop (at 454 N) is followed by a non-linear increase in load and results in the maximum load (P_{max}) of 603 N. At that point a rapid expansion of $a_{opening}$ was visible at the specimen surface. With increased load a stable crack growth with crack deflection at the fibres is visible on the surface. The maximum load is followed by a stepwise failure.

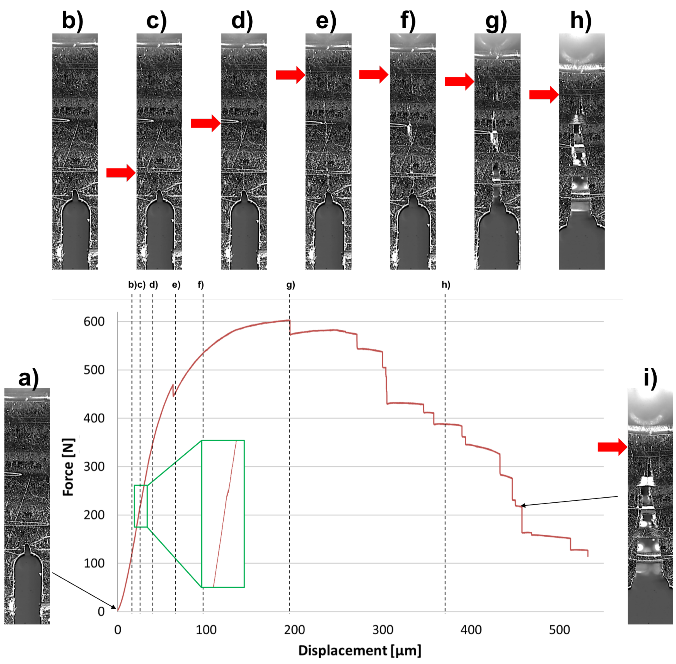

Figure 5: Load-displacement diagram for one as-fabricated specimen (No. 6). The rising load bearing capacity with surface crack growth and a large crack opening is visible. (a) 0 μm displacment/0 N load, b) 18 μm/139 N, c) 26 μm/220 N, d) 39 μm/346 N, e) 63 μm/448 N, f) 99 μm/540 N, g) 195 μm/603 N, h) 369 μm/388 N und i) 457 μm/217 N). The red arrows mark the crack tip in each picture.

During the loading of the embrittled sample a load drop at 146 N is observed (Fig. 6). This is followed by the maximum load P_{max} (154 N) and a large load drop. The crack growth during loading up to the maximum load could not be observed by the optical monitoring because, the surface roughness of the embrittled samples was to high: the samples were only polished before the heat treatment as it was done with all specimens. The composite was still able to bear some load after P_{max}.

After crack initiation the composite was, in both cases, still able to bear an increasing load. Therefore, the visible crack length was added to the initial crack length ($a_{initial}$), resulting in the surface crack length $a_{surface}$ (see Fig. 3 for clarification). Fig. 7 exemplifies the selection of the loads used for the fracture toughness evaluation. For $a_{surface}$ the maximum load was used as P (P_{max}) to calculate K_{max}. For the as-fabricated $W_f/W_{Y_2O_3}$ specimens the values before the first significant load-drop was used for further evaluations and is called P_Q. For the embrittled samples the maximum load and correlating $a_{surface}$ was used. The results for the fracture toughness evaluation are summarized in Tab. 3.

The mean K_{max} fracture toughness value for the as-fabricated

Table 4: Set of 3PB specimens of W_f/W used for J-Integral calculation. (Interlayer:Y_2O_3)

No.	B [mm]	H [mm]	$a_{initial}$ [mm]	a_{final} [mm]	$i_{crackstart}$ [–]	$J_{Q-initial}$ [kJ/m^2]	J_{Q-max} [kJ/m^2]	K_{J-max} [MPa m$^{1/2}$]
12	3.0	4.0	1.2	3.3	3	0.04	5.8	51.1
13	3.0	4.0	1.0	3.20	2	0.04	7.5	57.6
14	3.0	3.9	1.0	3.1	4	0.07	6.4	47.7
15	3.0	4.0	1.2	3.1	3	0.03	5.2	51.1
16	2.9	4.0	1.1	3.5	1	0.03	6.6	53.8

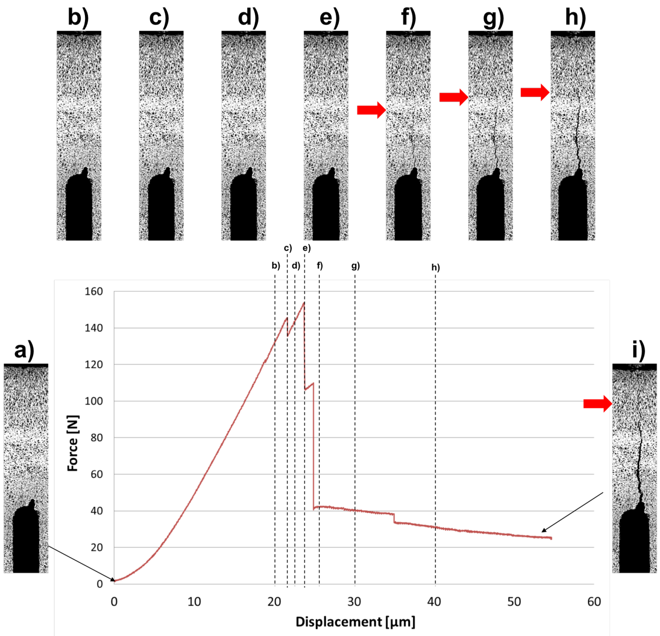

Figure 6: Load-displacement diagram for one embrittled specimens (No. 9). A rising load bearing after crack initiation is to be observed. The crack growth on the surface is observable after the maximum load. (a) 0 μm displacement/0 N load, b) 20 μm/133 N, c) 21,6 μm/146 N, d) 22 μm/139 N, e) 23,8 μm/107 N, f) 25 μm/41 N, g) 30 μm/40 N, h) 40 μm/31 N und i) 54 μm/26 N). The red arrows mark the crack tip in each picture.

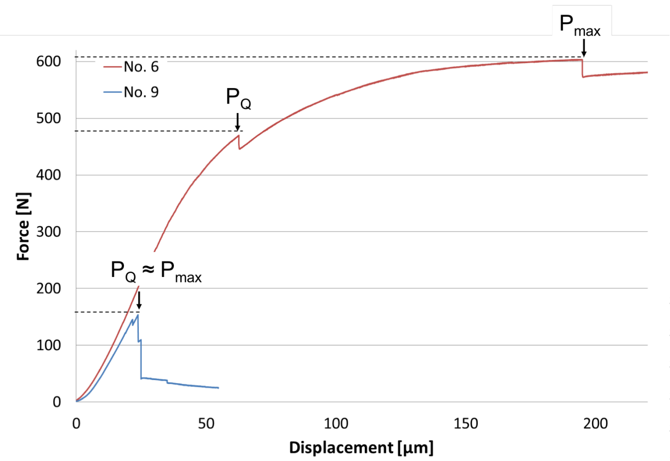

Figure 7: Load-displacement diagrams for one as-fabricated (No. 6: red) and one embrittled specimens (No. 9: blue). The loads P_Q and P_{max} which were taken for the K_P and K_{max} evaluation are shown.

$W_f/W_{Er_2O_3}$ is 161 ±30 MPa m$^{1/2}$, for the $W_f/W_{Y_2O_3}$ it is 206 ±29 MPa m$^{1/2}$. This is by one order of magnitude higher then the mean values of 15 ±5 MPa m$^{1/2}$ for $W_f/W_{Er_2O_3}$ and 14 ±1 MPa m$^{1/2}$ for $W_f/W_{Y_2O_3}$ in the embrittled case. No influence of the different heat treatments, interlayer material and fiber volume fractions was observed during the tests and evaluation.

The surface observation of the crack growth allowed to visualise the rising resistance against crack growth in a so called resistance-curve (R-Curve). The high quality optical measurement system was only available for the $W_f/W_{Y_2O_3}$ samples and no crack growth during loading up to the maximum load could be observed for the embrittled samples. Therefore, only the R-Curves for the $W_f/W_{Y_2O_3}$ samples were calculated. The values for the R-Curve were calculated by defining specific points on the load-displacement curves. At that points, the crack length was measured on the sample surface and the K values were calculated with the associated load. The calculated R-Curves for three specimens are shown in Fig. 8.

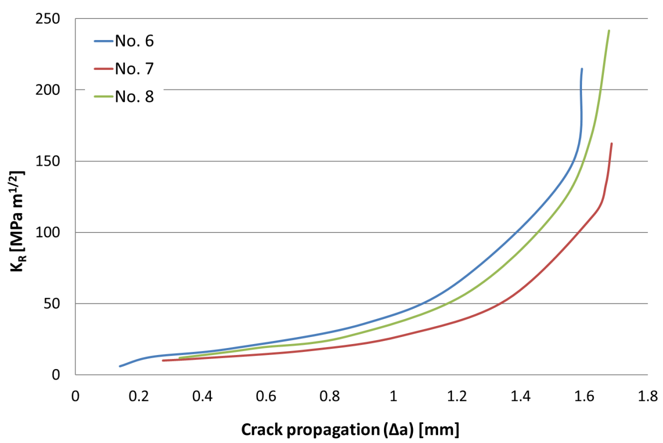

Figure 8: R-curve for $W_f/W_{Y_2O_3}$, tested according to ASTM399 in the as-fabricated state.

A typical fracture surface of the as-fabricated sample No. 6 with Y_2O_3 interlayer is shown in Fig. 9. This specimen shows only plastically deformed W fibres with the typically knife edge fracture (Fig. 9 c)) [32]. The W matrix in Fig. 9 a) is nearly fully dense (99.3 %) and the typical corona shape of the CVD-W [33, 34, 35] can be seen. Near the fibres, the matrix shows mainly intergranular fractureed small grains (Fig. 9 d), e)). Nearly all bigger W grains show transgranular fracture (Fig. 9 b)). The interlayer (in this case Y_2O_3) does not show any damage and sticks to the matrix (Fig. 9 b)-e)). Hence, the fibre is circumferentially fully debonded from the interlayer.

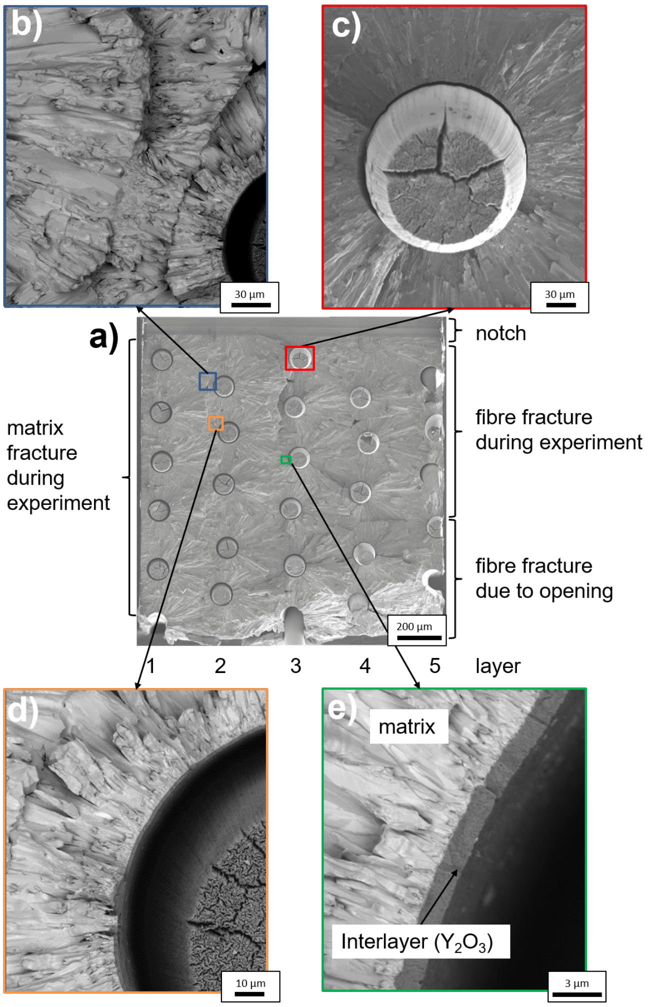

Figure 9: Typical fracture surface of specimen No. 6 with detailed views of the fractured matrix (b)), fractured fibre (c)) and the Y_2O_3 interlayer region (d), e)).

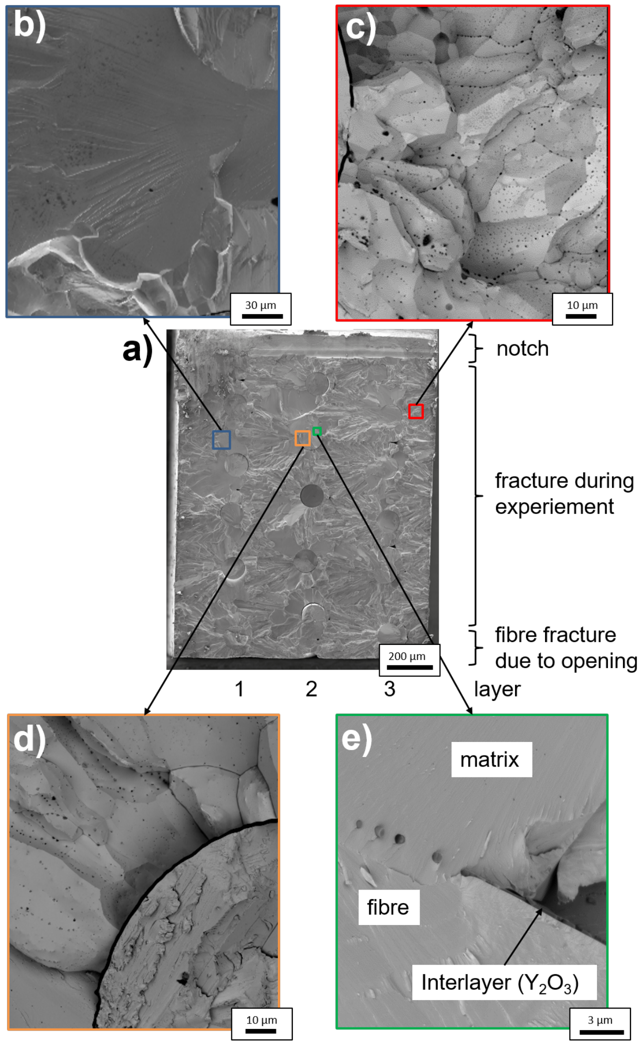

Figure 10: Typical fracture Surface of Specimen No. 9 with detailed views of the fractured matrix (b)), fractured matrix (c)) and the Y_2O_3 interlayer region (d), e)).

A typical fracture surface of an embrittled samples is shown in Fig. 10 (sample No. 9, Y_2O_3 interlayer). In that case all fibres in all specimens fractured brittle and showed mainly cleavage with scattered spots of intergranular fracture (Fig. 10 d)). In the matrix visible in Fig. 10 c), d), pores or bubbles at the fractured grain bounderies are visible. One possible explanation for the pores is the deposition of the fluorine of the precursor gas during the CVD process which leads to a pore formation during the heat treatment [36]. At these locations, the matrix fractured intergranular. The heated/embrittled W matrix showed more transgranular fracture as the W grains are bigger than in the as-fabricated state (Fig. 10 c)). The thickness of the Y_2O_3 interlayer is strongly reduced and on some spots grain growth from the matrix to the fibre was observed (Fig. 10 e)). This was not observed for Er_2O_3. Both interlayers (Er_2O_3 and Y_2O_3) were fractured and stick to the matrix as well as to the fibres (Fig. 10 d), e)).

3.2. *Results according to ASTM E1820 (J_Q)*

Fig. 11 shows the load-displacement diagram of the representative specimen No. 16.

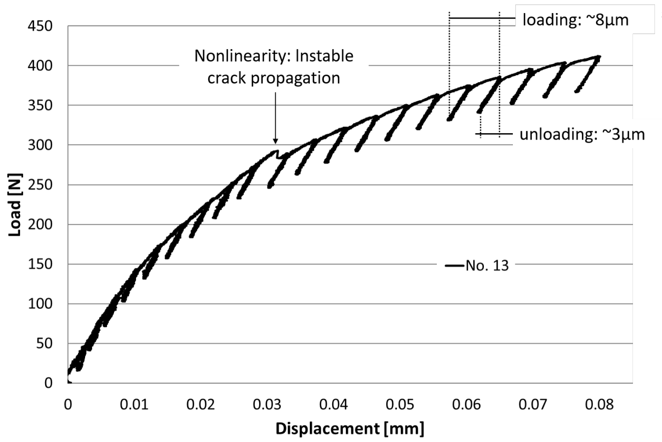

Figure 11: Typical load-displacement diagram of the J_Q test of Specimen No. 13. All specimens were cyclically loaded with a displacement of 8 μm followed by an unloading of 3 μm.

The only macroscopic drop visible in the curve appears due to an instable crack propagation. The J-values for crack initiation are measured to be $J_{Q-initial}$ = 0.04 ±0.02 kJ/m^2. The maximum J-values are J_{Q-max} = 6.3 ±0.9 kJ/m^2. The J-R-curves are similar for all specimens (Fig. 12). Only specimen No. 16 shows a slightly flatter J-R-curve. The crack growth on the surface is comparable with the $W_f/W_{Y_2O_3}$-K_P samples were with increased load a stable crack growth is visible on the surface. The provisional fracture toughness K_{J-max} was calculated for the maximum J_Q value J_{Q-max}. Tab. 4 summarises all the results for the J_Q evaluation.

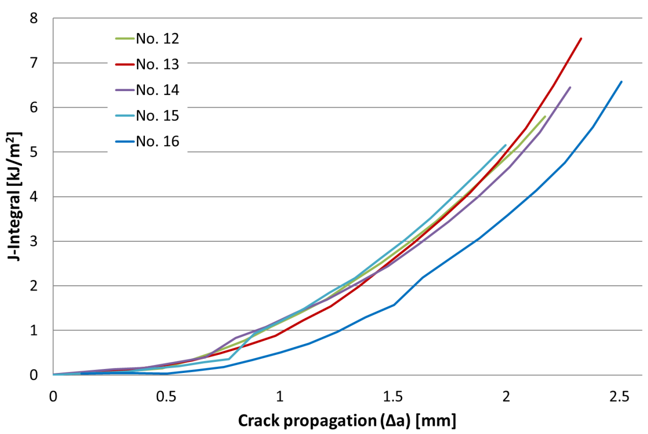

Figure 12: J-R-curves for the J-Integral test. The resistances against crack growth is growing with rising crack propagation.

Fig. 13 a) shows the fracture surfaces of the specimens No. 13 which had an optical density of almost 100 %. The fracture surface of specimen No. 16 with an optical density of 94 % is shown in Fig. 13 b). The red line marks the final crack tip. The fracture surfaces of all specimens show the typical corona shape of the CVD-W [33, 34]. In all cases more than 90 % transgranular fracture of the CVD-matrix can be observed. Only the small grains near the fibres show intergranular fracture. As $a_{opening}$ at the tests was below 30 μm (W fibre elongation at fracture: 51 μm [25]) no fibre was fractured during the test.

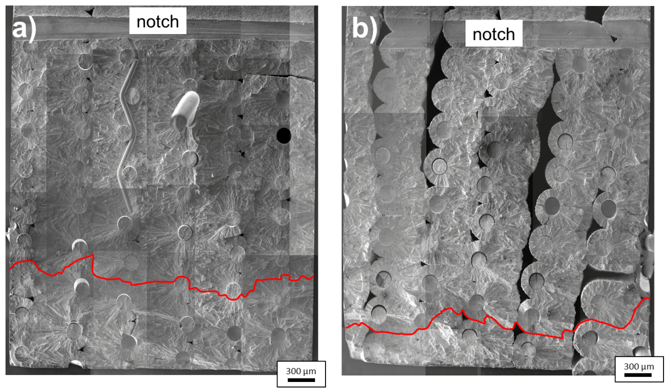

Figure 13: Fracture surface of specimen No. 13 (a)) and No. 16 (b)). The red line marks the crack front which was formed within the experiment. The cavities in the fracture surface of No. 16 (b) are unfilled pores which results in the high porosity.

The calculated fracture toughness values K_J corresponding different J-values at different crack length are shown in Tab. 5. This points were chosen as comparison to other materials [20, 21, 1]. The $K_{J-0.2}$ were calculated with the loads at a crack length of 0.2 mm and the $K_{J-1.5}$corresponds to the loads at a crack length of 1.5 mm.

Table 5: K_J calculation from different J values W_f/W.

No.	$J_{0.2}$ [kJ/m^2]	$K_{J-0.2}$ [MPa m$^{1/2}$]	$J_{1.5}$ [kJ/m^2]	$K_{J-1.5}$ [MPa m$^{1/2}$]
12	0.06	5.2	2.5	33.2
13	0.08	5.8	2.5	33.0
14	0.05	4.6	3.0	36.5
15	0.10	6.7	2.4	32.8
16	0.04	4.4	1.6	26.3

4. Discussion

4.1. *Discussion of K_P results*

As-fabricated samples

The representative curve of the as-fabricated sample (Fig. 5) showed a first load drop after elastic loading followed by a deviation from the elastic slope. This is followed by a further load drop before the curve begins to flatten and the maximum load is reached. More load drops can be seen after having reached maximum load until the composites breaks. In the present study, the microstructural investigation showed that the debonding for both interlayer materials (Er_2O_3 and Y_2O_3) is observed between fibre and interlayer and all fibres failed ductile with the typical necking and knife-edge fracture surface as described before [32]. Fibre pull out could not be observed caused as in a three point bending test the stress peak is in the centre of the specimen.

This behaviour is typical for tough composites reinforced with ductile fibres as shown for other composite materials in [37, 38, 39]. In such and in our materials, the first load drop corresponds to crack initiation in the matrix, the flattening of the curve is caused by the ductile deformation of the fibres, the ultimate load is determined by the strength of the fibres and the load drops are caused by multiple fibre fracture. These effects are all caused by extrinsic toughening mechanisms and the load transfer from the matrix to the fibres is governed by the interaction with the interlayer.

The extrinsic toughening mechanisms which are typically active in W_f/W were already found to be energy dissipation by fibre–matrix interface debonding and crack deflection, crack bridging by intact fibres, ductile deformation of fibres and pull out of fractured fibres from the matrix [13, 26, 40]. The first mechanisms which become active after crack initiation are debonding, crack deflection. Crack meandering has a only a low contribution to the load bearing capacity as load transfer is directly accomplished by the crack bridging of the intact fibres. The crack bridging is the main mechanism as long as the fibres are able to bear the rising load. Once the load exceeds the yield stress of the fibres ductile deformation takes place and the ductile deformation is assumed to be the dominant and most effective mechanism [13]. The fibres enable a large scale crack bridging due to their large fracture strain (compared to the matrix) as known from other composites [41, 42]. With increasing load and displacement the crack opening of the specimen is increasing.

As the mechanisms act behind the crack tip there is a large zone which can be seen as plastic zone behind the crack tip. In addition, the plane strain condition is not predominate in the crack tip from a certain crack opening on as the loading conditions changes. Therefore a valid plane strain fracture toughness cannot be calculated using the ASTM E399 at which this is a main requirement. To ensure that the plastic zone is small compared to the specimen cross section and therefore the specimen fracture under nominally linear elastic conditions [21], two size criteria from the ASTM E399 needs to be fulfilled to calculate the fracture toughness K_{IC}. The first criteria which defines the specimen height - crack length ratio is only be fulfilled if the K_{IC} is calculated with $a_{initial}$ (see Tab. 3). However, $a_{initial}$ is only the starting crack length and with increasing load, the crack is growing. The second size criterion (a and B $\geq$ 2.5 $\cdot$ $(K_P/\sigma_y)^2$) can be calculated with the tensile strength of 480 MPa for $W_f/W_{Er_2O_3}$ [17] and 231 MPa for $W_f/W_{Y_2O_3}$ [43]. Both size criteria given in the ASTM E399 cannot be considered as fulfilled for the as-fabricated case as the samples are too small.

If we look at small crack opening where bending in the specimen is small the plane stress state is still valid and the calculation of K_P values might be possible. To ensure small crack openings, the load P_Q (Fig. 7) was chosen to calculate K_P. The crack openings, the corresponding force values and the values of this calculations are shown Tab. 6.

Table 6: Crack opening and resulting $K_{P_{surface}}$ values for $W_f/W_{Y_2O_3}$ specimens.

No.	$a_{surface}$ [μm]	$a_{opening}$ [μm]	P [N]	K_P [MPa m$^{1/2}$]
6 - P_Q	2870	19	452	143
6 - P_{max}	2905	128	603	214
7 - P_Q	2900	27	460	133
7 - P_{max}	2920	128	538	162
8 - P_Q	2860	20	516	167
8- P_{max}	2940	103	611	241

Embrittled samples

The typical curve of the embrittled sample (Fig. 6) shows a linear loading and after a first load drop no deviation of the linear slope. This is followed by a linear rising of the load. After reaching the maximum a sharp drop in the load occurred. This is followed by further load drops before the material fails completely. The microstructural investigation of the tested sample shows interlayer debonding and that all fibres fractured brittle.

The mechanisms which are typically active in a embrittled W_f/W sample are fibre–matrix interface debonding and crack deflection, crack bridging by intact fibres and pull out of fractured fibres from the matrix [40]. Pull out is not active in a three point bending test as the stress peak is in the centre of the specimen and thus all fibres fail in the centre. In addition, the brittle fibres have a low fracture strain ($\sim$0.1 %) and low tensile strength (896 MPa)[22] which is comparable with the tungsten matrix [33]. As in the as-fabricated samples, the first mechanisms which become active after crack initiation are debonding, crack deflection and crack meandering. This is followed by crack bridging of intact fibres, this is the main mechanism in the embrittled state. Once the load exceeds the fracture stress of the fibres they are failing brittle.

After the first load drop the load transfer from the matrix to fibre is accomplished by the debonding and frictional interaction of the fibres with the interlayer material and the fibres which are bridging the crack by elastic deformation. As the fracture strain of the fibres is relatively low, the specimen crack opening (crack bridging of the fibres) and thus bending before fracture is relatively small. Hence, the plane strain condition is predominate in the crack tip and the derived fracture toughness can be considered as valid within standard ASTM E399.

Only for sample No. 5 the first size criteria can be achieved. As no data exists about the ultimate tensile strength of embrittled W_f/W the second size criteria is estimated using the tensile strength of the embrittled W-fibres [22] with the corresponding fibre fraction and the tensile strength of the matrix materials [44] . This results in the tensile strength of 253 - 448 MPa for $W_f/W_{Er_2O_3}$ and 306 - 404 MPa for $W_f/W_{Y_2O_3}$. The second size criteria can can be achieved for specimen No. 3 if calculated with 448 MPa. So, the plane strain condition, the first size criteria (for one specimen) and the second (for one specimen), are fulfilled and therefore the values for the embrittled case seems to be reliable.

4.2. Discussion of J-Integral testing and J_Q results

The J-Integral testing with the cyclic loading and unloading (Fig. 11) of the samples lead to a stable crack growth visible on the surface of the specimen. The loading of the specimen was stopped at crack openings between a minimum of 21 μm (No. 15) to a maximum of 29 μm (No. 13) to minimize bending at the crack tip and therefore achieve plane strain conditions at the crack tip. With these small openings the W fibres were only elastically loaded as the used W fibres (Ø 150 μm) have a lower yield elongation [25, 22]. As the elongation for failure is 57 μm [25], no fibre was fractured during the tests. This means that after the matrix fractured during the test, the crack was bridged by the elastically loaded fibres. In absence of ductile fibre deformation, the mechanisms active are energy dissipation by fibre–matrix interface debonding and crack deflection and the crack bridging by intact fibres. The main mechanism which contributes to the fracture toughness is the large scale crack bridging as know from other composites [41, 42]. In the as-fabricated case the contribution of the fibres is increasing with larger crack opening and thus the fracture toughness is also increasing. Larger crack openings needs to be seen in combination with the need of ensuring plane strain conditions at the crack tip. For that reason larger crack openings with plane strain conditions at the crack tip can only be achieved if the specimen size will be increased and thus bending in the crack tip will be minimized. In a next step larger specimens should be tested which will allow to load the fibres till failure and as the ductile fibre deformation is assumed to be the dominant mechanism [13] to calculate the maximum J_Q.

4.3. Fracture behaviour and consequences for W_f/W

The evaluated R-Curves (Fig. 8) and the J-R-curves (Fig. 12) have a concave shape without any plateaus. This is in contrast to the R-Curves for homogeneous ductile materials which show a convex shape with a plateau at larger crack lengths [21]. That means, that the resistance against crack growth in homogeneous ductile materials reaches a maximum value for a defined crack length. This is not the case for fibre reinforced composite and thus for W_f/W as the extrinsic toughening mechanism [26] become more and more active behind the crack tip and therefore the resistance against crack growth is rising as the crack is growing. This behaviour is caused by the large scale bridging conditions and known from other fibre reinforced composites [42]. Especially the crack bridging and ductile deformation of the fibres which become active at large crack openings are the major contribution to the toughening in the as-fabricated state.
Considering the materials properties, there is a degradation from the as-fabricated to the embrittled material. This can be seen in the fracture toughness values as well as in the appearance of the curves. The previous identification of the different active toughening mechanisms explains why the maximum load and the K_{max} are one order of magnitude lower in the embrittled case than in the as-fabricated case. The composite properties of the as-fabricated and embrittled composite are mainly defined by the properties of the fibres which superpose all other mechanisms active in the material. In as-fabricated conditions the strength of the interlayer can be neglected as long as it debonds: The fracture strain of the fibres is much higher than the fracture strain of the matrix and the fibres will always debond, independently of the strength of the interlayer, which is according to theory [45]. This is in contrast to the embrittled case where the fibre properties are degraded and the interlayer debonding is crucial for crack bridging [46] and the rising load bearing capacity. All so far tested interlayers were tested with as-fabricated material [9, 47, 48, 49, 50] but the further interlayer design needs to be optimized toward the embrittled, more crucial state.
A critical point in the shown evaluations is the validity of plane strain condition in the crack tip and the size criteria given in ASTM E399 and ASTM E1820. The plane strain condition seems to be valid in the embrittled samples as well as in the J-integral testing as in both cases the crack opening is small compared to the specimen height. Due to the materials behaviour of W_f/W and the strict regulations of the ASTM E399 (curve shape, specimen size etc.) this standard should not be applied for further toughness evaluations.

4.4. Comparison with tungsten and tungsten based materials

Tungsten and tungsten based materials show at RT a brittle fracture with an instable crack propagation leading to a complete fracture of the specimens. Due to the brittle nature of W and W based materials at RT the use of the ASTM E399 is an appropriate method to calculate the fracture toughness [18, 51, 52, 33]. This is in contrast to the here shown behaviour of W_f/W where stable crack propagation and a rising load bearing capacity after crack initiation was shown for as-fabricated and embrittled material at RT.
The crack initiation in the matrix of W_f/W starts at a value which is comparable to that of CVD-W with values of around 5 MPa $m^{1/2}$ [33]. As-fabricated W_f/W demonstrated a large contribution of the fibre ductility, the J-Integral should be applied for that case. The values calculated with the J-Integral are more than two times larger than the valid values calculated for polycrystalline tungsten at 400 °C [51].
Embrittled W_f/W has comparable fracture toughness values as observed in previous studies for W and W based materials [18, 51, 52, 33] and in addition stable crack growth.
As the load case of the material needs to be seen in combination with the active toughening mechanisms and the material behaviour, the pure fracture toughness values of W_f/W alone can hardly lead to material recommendation. In comparison to W, W_f/W has the advantage that already at temperatures where other W materials are brittle, stable crack propagation and crack stopping is possible. In addition, local overloads and fabrication flaws which causes stress peaks do not lead to a complete failure. This allows design rules as used for metals such as defining critical crack length and maximum fatigue cycle limits.

5. Summary and Conclusion

The aim of this work was to investigate the fracture behaviour and to get a first estimation for the fracture toughness (K_P and

J-Integral) of long fibre W_f/W in the as fabricated and embrittled state. According to the ASTM E399, a maximum value for the as-fabricated with K_{max}= 241 MPa $m^{1/2}$ and for the embrittled composites with K_{max}= 20.5 MPa $m^{1/2}$ was calculated. There was no difference in the material properties caused by the different heat treatments, interlayer materials and fiber volume fractions. As, the material showed as stable crack prorogation, the J-Integral approach according to ASTM E1820 was additionally applied to the as-fabricated state and a J_{Q-max}= 7.5 kJ/m^2 (57.6 MPa $m^{1/2}$) was determined. All this values need to be seen as provisional fracture toughness values as the specimens were to small to calculate valid fracture toughness values. The results showed, that the W_f/W behaviour is dominated by the fibre behaviour and the contribution of the fibres rises with larger crack openings. The composite showed stable crack propagation, crack deflection and crack stopping in the as-fabricated state. Due to the degradation of the fibre properties, ductile fibre deformation is not present in the embrittled W_f/W. This is directly correlated with the lower load embrittled W_f/W can withstand before failure. Therefore, the embrittled state needs to be seen as the critical state of the material and for example the interlayer needs to be designed for that state.
As a next step larger specimens should be tested with the J-Integral method in order to be able to investigate larger crack openings under plane strain condition in the crack tip (minimal bending during J-Integral testing), were the fibres have a more significant contribution to the material behaviour.

Acknowledgement

The authors want to acknowledge the Osram GmbH, Schwabmünchen, Germany for providing the W fibres and the whole W_f/W team in Jülich and Garching, especially Leonard Raumann and Yiran Mao for their help during the W_f/W fabrication. Moreover, the support of Gabriele Matern, Stefan Elgeti and Martin Balden with the sample preparation especially the FIB milling was very helpful. This work has been carried out within the framework of the EUROfusion Consortium and has received funding from the Euratom research and training programme 2014-2018 and 2019-2020 under grant agreement No 633053. The views and opinions expressed herein do not necessarily reflect those of the European Commission.

References

[1] ASTM E1820 - 09: Standard Test Method for Measurement of Fracture Toughness, 2013.

[2] E399 - 90: Standard Test Method for Plane-Strain Fracture Toughness of Metallic Materials.

[3] J.W. Coenen, S. Antusch, M. Aumann, W. Biel, J. Du, J. Engels, S. Heuer, A. Houben, T. Höschen, B. Jasper, F. Koch, J. Linke, A. Litnovsky, Y. Mao, R. Neu, G. Pintsuk, J. Riesch, M. Rasinski, J. Reiser, M. Rieth, A. Terra, B. Unterberg, Th. Weber, T. Wegener, J.-H. You, and Ch. Linsmeier. Materials for DEMO and reactor applications boundary conditions and new concepts. *Physica Scripta*, T167:014002, 2016.

[4] C. Gandhi and M.F. Ashby. Overview no. 5: Fracture-mechanism maps for materials which cleave: F.C.C., B.C.C. and H.C.P. metals and ceramics. *Acta Metallurgica*, 27(10):1565–1602, 1979.

[5] E. Lassner and W.-D. Schubert. *Tungsten - Properties, Chemistry, Technology of the Element, Alloys, and Chemical Compound*. Springer, 1999.

[6] W. Yih and C. Wang. *Tungsten: Sources, Metallurgy, Properties, and Applications*. Springer US, 1979.

[7] V. Barabash, G. Federici, M. Rödig, L. Snead, and C. Wu. Neutron irradiation effects on plasma facing materials. *Journal of Nuclear Materials*, 283-287:138–146, 2000.

[8] J.M. Steichen. Tensile properties of neutron irradiated TZM and tungsten. *Journal of Nuclear Materials*, 60:13–19, 1976.

[9] B. Jasper, S. Schönen, J. Du, T. Höschen, F. Koch, C. Linsmeier, R. Neu, J. Riesch, A. Terra, and J.W. Coenen. Behavior of tungsten fiber-reinforced tungsten based on single fiber push-out study. *Nuclear Materials and Energy*, 9:416–421, 2016.

[10] Y. Mao, J.W. Coenen, J. Riesch, S. Sistla, J. Almannstötter, B. Jasper, A. Terra, T. Höschen, H. Gietl, M. Bram, J. Gonzalez-Julian, C. Linsmeier, and C. Bröckmann. Development and characterization of powder metallurgically produced discontinuous tungsten fiber reinforced tungsten composites. *Physica Scripta*, (T170):014005, 2017.

[11] R. Neu, J. Riesch, A.v. Müller, M. Balden, J.W. Coenen, H. Gietl, T. Höschen, M. Li, S. Wurster, and J.-H. You. Tungsten fibre-reinforced composites for advanced plasma facing components. *Nuclear Materials and Energy*, 12:1308–1313, 2016.

[12] J. Riesch, M. Aumann, J.W. Coenen, H. Gietl, G. Holzner, T. Höschen, P. Huber, M. Li, Ch. Linsmeier, and R. Neu. Chemically deposited tungsten fibre-reinforced tungsten - the way to a mock-up for divertor applications. *Nuclear Materials and Energy*, 9:75–83, 2016.

[13] J. Riesch, T. Höschen, Ch. Linsmeier, S. Wurster, and J.-H. You. Enhanced toughness and stable crack propagation in a novel tungsten fibre-reinforced tungsten composite produced by chemical vapour infiltration. *Physica Scripta*, T159:014031, 2014.

[14] J.W. Coenen, Y. Mao, J. Almannstötter, A. Calvo, S. Sistla, H. Gietl, B. Jasper, J. Riesch, M. Rieth, G. Pintsuk, F. Klein, A. Litnovsky, A.v. Müller, T. Wegener, J.-H. You, C. Bröckmann, C. Garcia-Rosales, R. Neu, and C. Linsmeier. Advanced materials for a damage resilient divertor concept for DEMO: Powder-metallurgical tungsten-fibre reinforced tungsten. *Fusion Engineering and Design*, 124:964–968, 2016.

[15] A.G. Evans. Perspective on the development of high-toughness ceramics. *Journal of American Ceramic Society*, 73:187–206, 1990.

[16] R. Neu, J. Riesch, J.W. Coenen, J. Brinkmann, A. Calvo, S. Elgeti, C. Garcia-Rosales, H. Greuner, T. Höschen, G. Holzner, F. Klein, F. Koch, Ch. Linsmeier, A. Litnovsky, T. Wegener, S. Wurster, and J.-H. You. Advanced tungsten materials for plasma-facing components of DEMO and fusion power plants. *Fusion Engineering and Design*, 109-111: Part A:1046–1052, 2016.

[17] H. Gietl, J. Riesch, J.W. Coenen, T. Höschen, C. Linsmeier, and R. Neu. Tensile deformation behavior of tungsten fibre-reinforced tungsten composite specimens in as-fabricated state. *Fusion Engineering and Design*, 124:396–400, 2016.

[18] S. Wurster, B. Gludovatz, A. Hoffmann, and R. Pippan. Fracture behaviour of tungsten-vanadium and tungsten-tantalum alloys and composites. *Journal of Nuclear Materials*, 413:166–176, 2011.

[19] J.R. Rice. A path independent integral and the approximate analysis of strain concentration by notches and cracks. *Journal of Applied Mechanics*, 35(2):379–386, 1968.

[20] E. Gaganidze and J. Aktaa. Use of the failure assessment diagram to deduce ductile fracture toughness of the RAFM steel EUROFER97. *International Journal of Pressure Vessels and Piping*, 86:345–350, 2009.

[21] T.L. Anderson. *Fracture Mechanics: Fundamentals and Applications*. CRC Press, Taylor and Francis Group, 3. edition, 2005.

[22] P. Zhao, J. Riesch, T. Höschen, J. Almannstötter, M. Balden, J.W. Coenen, U. Himml, U. von Toussaint, and R. Neu. Microstructure, mechanical behavior and fracture of pure tungsten wires after different heat treatments. *International Journal of Refractory Metals and Hard Materials*, 68:29–40, 2017.

[23] J. Du. *A feasibility study of tungsten-fiber-reinforced tungsten composites with engineered interfaces*. PhD thesis, Technische Universität München, 2010.

[24] H. Gietl, A.v. Müller, J. Riesch, J.W. Coenen, T. Höschen, Ph. Huber, M. Decius, D. Ewert, M. Milwich, and R. Neu. Textile techniques for tungsten fibre-reinforced composites production. *Journal of Composite Materials*, 52(28):3875–3884, 2018.

[25] J. Riesch, J. Almannstötter, J.W. Coenen, M. Fuhr, H. Gietl, Y. Han, T. Höschen, Ch. Linsmeier, N. Travitzky, and P. Zhao. Properties of

drawn W wire used as high performance fibre in tungsten fibre-reinforced tungsten composite. *IOP Conference Series: Materials Science and Engineering*, 136:012043, 2016.

[26] J. Riesch, Y. Han, J. Almannstötter, J.W. Coenen, T. Höschen, B. Jasper, P. Zhao, Ch. Linsmeier, and R. Neu. Development of tungsten fibre-reinforced tungsten composites towards their use in DEMO - potassium doped tungsten wire. *Physica Scripta*, T167:014006, 2016.

[27] Y. Mao, J.W. Coenen, J. Riesch, S. Sistla, J. Almanstötter, B. Jasper, A. Terra, T. Höschen, H. Gietl, Ch. Linsmeier, and C. Bröckmann. Influence of the interface strength on the mechanical properties of discontinuous tungsten fiber-reinforced tungsten composites produced by field assisted sintering technology. *Composites Part A: Applied Science and Manufacturing*, 107:342–353, 2018.

[28] A.v. Müller, M. Ilg, H. Gietl, T. Höschen, R. Neu, G. Pintsuk, J. Riesch, U. Siefken, and J.-H. You. The effects of heat treatment at temperatures of 1100 °C to 1300 °C on the tensile properties of high-strength drawn tungsten fibres. *Nuclear Materials and Energy*, 16:163–167, 2018.

[29] D.B. Marshall, B.N. Cox, and A.G. Evans. The mechanics of matrix cracking in brittle matrix fiber composites. *Acta Metallurgica*, 33:2013–2021, 1985.

[30] D. Gross and T. Seelig. *Bruchmechanik - Mit einer Einführung in die Mikromechanik*. Springer Verlag, 2016.

[31] A.G. Evans and D.B. Marshall. The mechanical behavior of ceramic matrix composites. *Acta Metallurgica*, 37:2567–2583, 1989.

[32] S. Leber, J. Tavernelli, and D.D. White. Fracture modes in tungsten wire. *Journal of the Less Common Metals*, 48:119–133, 1976.

[33] J.D. Murphy, A. Giannattasio, Z. Yao, C.J.D. Hetherington, P.D. Nellist, and S.G. Roberts. The mechanical properties of tungsten grown by chemical vapour deposition. *Journal of Nuclear Materials*, 386-388:583–586, 2009.

[34] W.A. Bryant. The fundamentals of chemical vapour deposition. *Journal of Materials Science*, 12(7):1285–1306, 1977.

[35] H. Gietl, J.W. Riesch, J.W. Coenen, T. Höschen, and R. Neu. Production of tungsten-fibre reinforced tungsten composite by a novel continuous chemical vapour deposition process. *Fusion Engineering and Design*, 146:1426–1430, 2019.

[36] W.A. Bryant. High-temperature strength stability of three forms of chemically vapor deposited tungsten. *Journal of Vacuum Science and Technology*, 11, 1974.

[37] T.M. Besmann, B.W. Sheldon, R.A. Lowden, and D.P. Stinton. Vapor-phase fabrication and properties of continuous-filament ceramic composites. *Science*, 253(5024):1104–1109, 1991.

[38] H.E. Deve and M.J. Maloney. On the toughening of intermetallics with ductile fibers: role of interfaces. *Acta Metallurgica et Materialia*, 39(10):2275–2284, 1991.

[39] H.E. Dève and S. Schmauder. Role of interface properties on the toughness of brittle matrix composites reinforced with ductile fibers. *Journal of materials research*, 7(11):3132–3138, 1992.

[40] J. Riesch, J.Y. Buffiere, T. Höschen, M. Scheel, Ch. Linsmeier, and J.-H. You. Crack bridging in as-fabricated and embrittled tungsten single fibre-reinforced tungsten composites shown by a novel in-situ high energy synchrotron tomography bending test. *Nuclear Materials and Energy*, 15:1–12, 2018.

[41] A.G. Evans and F.W. Zok. The physics and mechanics of fibre-reinforced brittle matrix composites. *Journal of Materials Science*, 29:3857–3896, 1994.

[42] D.R. Bloyer, R.O. Ritchie, and K.T. Venkateswara Rao. Fracture toughness and R-curve behavior of laminated brittle-matrix composites. *Metallurgical and Materials Transactions A*, 29(10):2483–2496, 1998.

[43] H. Gietl. *Weiterentwicklung von wolframfaserverstärktem Wolframverbundwerkstoff für den Einsatz in der Fusion*. PhD thesis, Technische Universität München, 2018.

[44] W. R. Holman and F. J. Huegel. Cvd tungsten and tungsten-rhenium alloys for structural applications. part ii. evaluation. In *pp 427-58 of Proceedings of the Conference on Chemical Vapor Deposition of Refractory Metals, Alloys, and Compounds, Gatlinburg, Tennessee, September 12–14, 1967. Schaffhauser, AC (ed.). Hinsd*. Univ. of California, Livermore, 1968.

[45] M.-Y. He and J.W. Hutchinson. Crack deflection at an interface between dissimilar elastic materials. *International Journal of Solids and Structures*, 25:1053–1067, 1989.

[46] J. B. Wachtman, W. R. Cannon, and Matthewson M. J. *Mechanical Properties of Ceramics*. 2. edition, 2009.

[47] H. Gietl, J. Riesch, J.W. Coenen, T. Höschen, M. Zielinski, and R. Neu. Comparison of interfacial shear strength of tungsten fibre-reinforced composites evaluated with different methods. *In Preperation*, 2019.

[48] J. Du, T. Höschen, M. Rasinski, S. Wurster, W. Grosinger, and J.-H. You. Feasibility study of a tungsten wire-reinforced tungsten matrix composite with ZrOx interfacial coatings. *Composites Science and Technology*, 70:1482–1489, 2010.

[49] J. Du, T. Höschen, M. Rasinski, and J.-H. You. Shear debonding behavior of a carbon-coated interface in a tungsten fiber-reinforced tungsten matrix composite. *Journal of Nuclear Materials*, 417:472–476, 2011.

[50] J. Du, T. Höschen, and J.-H. You. Thermal stability of the engineered interfaces in W_f/W composites. *Journal of Materials Science*, 47:4706–4715, 2012.

[51] E. Gaganidze, D. Rupp, and J. Aktaa. Fracture behaviour of polycrystalline tungsten. *Journal of Nuclear Materials*, 446:240–245, 2014.

[52] B. Gludovatz, S. Wurster, A. Hoffmann, and R. Pippan. Fracture toughness of polycrystalline tungsten alloys. *International Journal of Refractory Metals and Hard Materials*, 28(6):674–678, 2010.